Influence of alumina addition on steam corrosion behaviour of ytterbium disilicates for environmental barrier coating applications

Corrosion Science 207 (2022) 110555

Contents lists available at ScienceDirect

Corrosion Science

journal homepage: www.elsevier.com/locate/corsci

Influence of alumina addition on steam corrosion behaviour of ytterbium disilicates for environmental barrier coating applications

Ahmet Hilmi Paksoy [a], Joao P. Martins [a], Huatang Cao [a], Ying Chen [a], Grant Gibson [b], Ping Xiao [a,*]

[a] University of Manchester, Department of Materials, Henry Royce Institute, Manchester M13 9PL, UK
[b] Surface Engineering, Rolls-Royce Plc, Derby DE24 8BJ, UK

ARTICLE INFO

Keywords:
Environmental barrier coatings
Silicate
Sintering
Steam corrosion

ABSTRACT

The sintering and steam corrosion behaviour of $Yb_2Si_2O_7$ with and without the addition of Al_2O_3 has been studied on compacted specimens. While, the addition of Al_2O_3 to $Yb_2Si_2O_7$ enhanced the sintering of $Yb_2Si_2O_7$ significantly, it also promoted the formation of a thin (80–100 nm), dense and protective $Yb_3Al_5O_{12}$ layer at the $Yb_2Si_2O_7$ surface when exposed to steam. TEM analysis confirmed that the $Yb_3Al_5O_{12}$ layer is formed in steam environment via surface diffusion of aluminium from residual Al_2O_3 present on the surface of $Al_2O_3/Yb_2Si_2O_7$ composite. These findings demonstrate the benefit of Al_2O_3 addition to protect environmental barrier coatings from steam corrosion.

1. Introduction

Silicon carbide-based ceramic matrix composites (SiC-CMC) have emerged as one of the most reliable alternatives for next-generation gas turbines [1,2]. Although CMCs exhibit excellent oxidation resistance in dry oxygen environments, given the formation of a protective silica scale at elevated temperatures, in steam environments the silica scale reacts to form volatile Si-O-H species [3,4]. Therefore, environmental barrier coatings (EBCs), typically comprised of a silicon bond coat and ceramic topcoat layers, are applied to protect CMCs from the steam environment.

Rare-earth disilicates ($RE_2Si_2O_7$) and rare-earth monosilicates (RE_2SiO_5) have been identified as the most promising materials for the EBC top coat since they meet most of the aforementioned requirements. Ytterbium disilicate ($Yb_2Si_2O_7$, hereafter referred to as YbDS) has received more attention because of its intrinsic high temperature phase stability and similar thermal expansion coefficient to SiC ($3.3 \times 10^{-6}\ K^{-1} \leq CTE_{YbDS} \leq 5.2 \times 10^{-6}\ K^{-1}$ and $3.5 \times 10^{-6}\ K^{-1} \leq CTE_{SiC} \leq 5.1 \times 10^{-6}\ K^{-1}$) [5]. However, the major drawback of YbDS is its insufficient steam corrosion resistance. According to the reaction given in Eq. (1), the depletion of silica in a high-temperature steam environment results in the formation of a porous ytterbium monosilicate (Yb_2SiO_5, hereafter referred to as YbMS) layer and surface cracks, due to an approximate 25% reduction in the unit cell volume; [6,7].

$$Yb_2Si_2O_7\ (s) + 2\ H_2O\ (g) \rightarrow Yb_2SiO_5\ (s) + Si(OH)_4\ (g) \quad (1)$$

Several studies have demonstrated the insufficiency of this porous YbMS in terms of steam corrosion protection to underlying coating layers sections and substrates [8,9]. Over the durations of steam exposure, oxidative species (i.e. oxygen and water vapour) were found to diffuse primarily through pores and grain boundaries of the YbDS and led to formation and thickening of a thermally grown oxide (TGO) at the interface between the silicon bond coat and EBC. Although the TGO layer acts as a diffusion barrier, cracking of the TGO during thermal cycling conditions is considered detrimental for coating systems [10]. Therefore, many attempts have been made to increase the density and corrosion resistance of YbDS based EBCs by altering the composition. Lee et al.[11] studied the effect of various oxide additives (i.e. Al_2O_3, TiO_2, mullite etc.) to air plasma sprayed (APS) EBCs on the TGO growth rate and found an 80% reduction in the thickness of the TGO layer for aluminium containing coatings in comparison to baseline EBC composed of just YbDS. The main reasons for increased steam corrosion resistance were reported as (i) reducing oxidant permeability through the EBCs due to accelerated sintering of Yb-Al silicates (ii) hindrance of oxygen diffusion through the aluminium modified SiO_2 network structure.

According to the ternary phase diagram of Yb_2O_3, Al_2O_3 and SiO_2 [12], YbDS reacts with Al_2O_3 at elevated temperature to form ytterbium alumina garnet ($Yb_3Al_5O_{12}$, hereafter referred to as YbAG), a material that has great potential for high-temperature applications such as

* Corresponding author.
E-mail address: p.xiao@manhcester.ac.uk (P. Xiao).

https://doi.org/10.1016/j.corsci.2022.110555
Received 17 April 2022; Received in revised form 29 July 2022; Accepted 30 July 2022
Available online 1 August 2022

thermal barrier coatings (TBC) or EBCs due to very high melting temperature (~2000 °C) and superior mechanical properties [13]. In addition, YbAG's excellent steam corrosion resistance makes YbAG a promising material to be used together with ytterbium based silicates [14,15]. Dong et al. [16] infiltrated metallic aluminium on YbMS EBCs and formed a dense oxygen barrier layer after heat treatment at 1100 °C. The formation of Al_2O_3 and YbAG phases was found to provide oxidation protection to the EBCs; however, their study did not investigate the steam corrosion behaviour of these coatings.

In this work, the Al_2O_3 addition was used initially to promote sintering of YbDS in compacted powder specimens, and then the steam corrosion resistance was investigated. Surprisingly, the addition of 3 wt % Al_2O_3 to YbDS led to formation of a YbAG thin layer at the surface of YbDS after being exposed to steam. The YbAG layer prevented further steam corrosion of the YbDS with inclusion of 3 wt% Al_2O_3 which contrasts to the results obtained for YbDS without addition of Al_2O_3 where transformation from YbDS to YbMS continued with steam exposure.

2. Materials and method

2.1. Fabrication and sintering of the specimens

YbDS (Treibacher Industrie AG) and aluminium oxide – Al_2O_3 (Alfa Aesar) powders were selected for this study as the primary material and sintering aid, respectively. For the composite specimens 1.5 wt%, 3 wt% and 5 wt% Al_2O_3 added to the YbDS powder (Composite specimens were hereafter referred to as YbDS/1.5Al_2O_3, YbDS/3Al_2O_3, and YbDS/5Al_2O_3 regarding to their alumina ratio respectively). Starting powders were ball-milled in a Teflon jar (with zirconia milling media and ethanol in a ratio of 1:1:2; powder:ethanol:zirconia) for 20 h to decrease the initial particle size and obtain a homogenous mixture. Thereafter, milled powders were dried for 24 h at 80 °C to evaporate the solvent and subsequently sieved to avoid powder agglomeration. The obtained powders were loaded into a 13 mm diameter steel die and uniaxially pressed under 150 MPa at room temperature for 20 s. The resulting cylindrical compacted specimens with 3 mm height were then sintered under atmospheric conditions at 1450 °C for 20 h with heating and cooling rates of 10 °C/min.

2.2. High temperature steam corrosion test

Prior to steam exposure, the surface of all the as-sintered specimens were polished down to 0.25 μm diamond grits. Specimens were then placed on a zirconia crucible, and the subsequent steam corrosion tests were conducted in an alumina tube furnace (RHF-1600 Carbolite) at 1350 °C for 20 h and 40 h in a 95% H_2O and 5% air environment with a gas velocity of ~19 cm/min. Heated steam was only introduced when the furnace reached to 1350 °C and stopped at the end of the exposure time. Assuming mixed gas temperature of 1350 °C, atmospheric pressure condition inside furnace tube and no pressure change in the system, 3 ml/min water flowrate and 190 ml/min air flowrate were set to achieve a 95/5 water vapour to air ratio based on the perfect gas law.

2.3. Characterisation

The weight change was measured using an analytical balance (± 0.001 g) prior to and after steam exposure for each specimen. The thickness of the corrosion layer after the steam exposure was measured from cross-sectional micrographs. The surface porosity of the as-sintered and steam exposed specimens was measured by determining the contrast difference in micrographs viewed with ImageJ software [17]. The phase compositions of the as-sintered and steam exposed specimens were evaluated using a The PANalytical X'Pert Pro X-Ray diffractometer. The instrument was operated at 40 keV and 40 mA with Cu-Kα radiation between 2Θ angles of 15° and 45° using a step size of 0.02°. The scanned XRD patterns were fitted using Rietveld analysis to determine the phase compositions [18]. Scanning electron microscope (SEM) (TESCAN Mira3 FEGSEM) equipped with energy dispersive spectroscopy (EDS-Oxford Instruments) was utilised to examine the effect of the Al_2O_3 addition on grain morphology and evolution of the microstructures upon steam exposure at 1350 °C.

Thin lamellae were machined by focused ion beam (FIB) (FEI Helios 660) at the intersection of several grains on the steam exposed, Al_2O_3 containing specimen to analyse the cross-sectional microstructure. Transmission electron microscopes (TEM) FEI Talos F200A (Analytical S/TEM equipped with Super-X 4 SDDs) and FEI Titan FEI Titan G2 80–200, both operated at 200 kV were used to examine the outermost layer. The phase compositions through the FIB lamellae were determined using selected area diffraction patterns (SAD) and energy-dispersive X-ray spectroscopy (EDS) images.

3. Results

3.1. Phase analysis and microstructural characterisation of as-sintered specimens

Fig. 1 shows X-ray diffraction patterns and quantification of the respective phase content of the as-sintered YbDS and Al_2O_3 added specimens. The main phase detected in all specimens was YbDS (ICDD # 04–007–4857). However, the specimens containing Al_2O_3 displayed an additional peak at 18° of 2θ diffraction angle (Fig. 1), which has been indexed as YbAG (ICDD # 01–073–1369). The presence of YbAG can be attributed to following reaction between YbDS and Al_2O_3 at elevated temperatures:

$$3Yb_2Si_2O_{7(s)} + 5\ Al_2O_{3(s)} \rightarrow 2Yb_3Al_5O_{12(s)} + 6SiO_{2(s)} \quad (2)$$

In addition, some low intensity Al_2O_3 peaks (ICDD # 04–015–8608) were also identified primarily in the YbDS/3Al_2O_3 and YbDS/5Al_2O_3 specimens. This result suggests that not all the Al_2O_3 reacted with YbDS to form YbAG and therefore residual Al_2O_3 grains may be present in the microstructure after initial sintering at 1450 °C for 20 h.

Fig. 2 shows the surface microstructures of YbDS with and without Al_2O_3 addition after initial sintering at 1450 °C for 20 h. YbDS without Al_2O_3 addition exhibited a very small but homogenous grain size (0.80 μm ± 0.06 μm) combined with an approximate porosity of 7 vol %. The YbDS/Al_2O_3 composite specimens displayed a dense microstructure (open pores could not be detected via image analysis) that

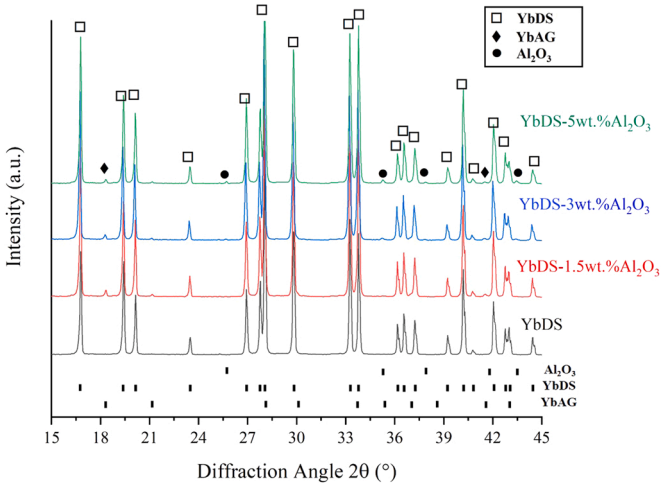

Fig. 1. XRD patterns of YbDS and YbDS/Al_2O_3 composites after initial sintering at 1450 °C for 20 h. The peak positions for YbDS, YbMS, YbAG and Al_2O_3 are based on the reference diffraction data displayed below the XRD patterns of specimens.

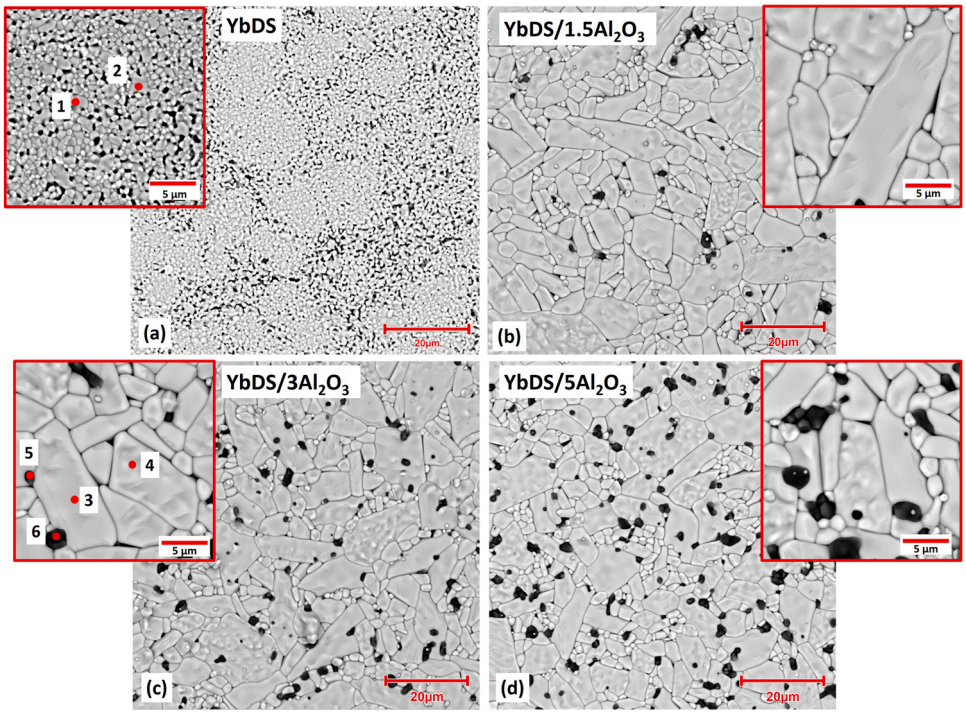

Fig. 2. Surface BSE-SEM micrographs after sintering at 1450 °C for 20 h (a) YbDS (together with high magnification inset image) consisting of 7 vol% porosity and grain in size of 0.8 µm ± 0.06 µm. (b) 1.5 wt% Al_2O_3, (c) 3 wt% Al_2O_3, (d) 5 wt% Al_2O_3 added composite compacts and inset high magnification images showing larger grain size of YbDS in flat-faced morphology and second phase presence. EDX confirmed that darker contrast phase corresponds to Al_2O_3.

consisted of larger YbDS grains in flat-faced morphology (i.e. facetted edges with round corners). The YbDS grains in the Al_2O_3 containing specimens can be categorised into grain size (GS); (i) GS > 10 µm, (ii) GS < 10 µm. The increase in alumina addition to YbDS originated an increased ratio of smaller grains to larger grains, as depicted in Fig. 2. Hence, the average value and standard deviation for a grain size of the composite compacts were found to be in decreasing tendency with the increase of alumina in the composition (Table 1). This phenomenon can be attributed to the boundary drag effect of Al_2O_3 to limit the grain growth.

The darker grains observed in the backscatter electron (BSE) micrographs of the composite specimen in Fig. 2-b to d indicates the presence of an additional phase to the already expected YbDS. Since the BSE detector is sensitive to the atomic number and electron interaction volume selected, a darker colouration is indicative of a lower average atomic number. Although, the XRD results in Fig. 1 confirmed that YbDS, YbAG and Al_2O_3 were the only phases present in the as-sintered microstructure, their similar average atomic numbers have likely prevented YbAG grains from being differentiated from YbDS in the BSE micrographs. The exclusion of principles therefore suggests that dark grains are residual Al_2O_3 that has not reacted with YbDS during the sintering process (Fig. 2-b, c and d). EDS analysis on the spots marked in Fig. 2-a and c are given in the Table 2. On the surface of the Al_2O_3 free specimen, only ytterbium, silicon and oxygen could be identified with the elemental ratios corresponding to YbDS (Spots 1 and 2). For the YbDS/$3Al_2O_3$ composite specimen, while the elemental ratio in the matrix corresponded to the YbDS (Spots 3 and 4), the darker grains were determined as Al_2O_3 (Spots 5 and 6). This finding supports the statement that residual Al_2O_3 grains (not reacted with YbDS during sintering) were present on the surface of the YbDS/$3Al_2O_3$ composite specimen.

Table 1
Average grain size of the YbDS on as-sintered compacts respect to Al_2O_3 concentration.

Compact Identity	Average Grain Size (µm)
YbDS	0.8 ± 0.06
YbDS/1.5Al_2O_3	17.3 ± 45.3
YbDS/3Al_2O_3	13.6 ± 28.9
YbDS/5Al_2O_3	9.6 ± 18.8

Table 2
Elemental composition of the spots locations highlighted in Fig. 2-a and c obtained via EDS analysis, and the corresponding phases.

	Elemental Composition (at%)				Corresponding Phase
Spot#	O	Yb	Si	Al	
1	60.3	20.7	19	N/D	YbDS
2	63	18.6	18.4	N/D	YbDS
3	60.1	20.8	19.1	N/D	YbDS
4	62.4	18.9	18.7	N/D	YbDS
5	59.2	N/D	N/D	40.8	Al_2O_3
6	59.1	N/D	N/D	40.9	Al_2O_3

N/D: Not detected

The 1.5 wt% addition in the sintered sample shows inhomogeneity in the grain size distribution of YbDS; ranging from 40 µm to submicron (Fig. 2-b). With the 5 wt% added specimen, too many residual alumina grains were found, which may result in generation of stress in the sintered sample due to much higher CTE of Al_2O_3 in comparison to YbDS ($CTE_{Al2O3} = 7.2 - 9.1 \times 10^{-6}\ K^{-1}$, $CTE_{YbDS} = 3.3 - 5.2 \times 10^{-6}\ K^{-1}$). Therefore, 3 wt% Al_2O_3 addition with relatively more uniform grain size and less Al_2O_3 residue was selected to study steam corrosion behaviour.

3.2. Effect of high temperature steam exposure on YbDS and YbDS/3Al_2O_3 specimen

3.2.1. Phase evolution

The X-ray diffraction patterns and phase ratios on the surface of the YbDS and YbDS/$3Al_2O_3$ specimens are presented in Fig. 3 after 20 h and 40 h of steam exposure. Fig. 3-a shows that for the YbDS specimen, a YbMS phase formed after 20 h of steam exposure and the peak

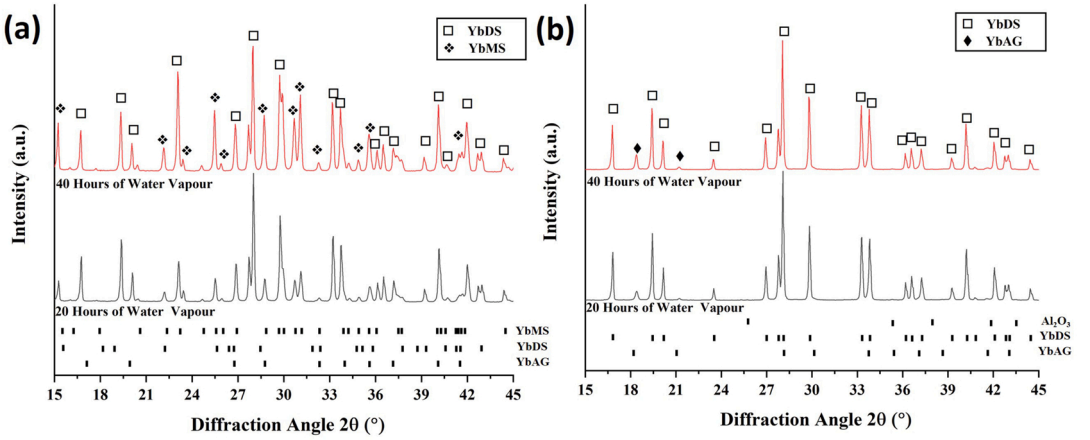

Steam Exposure Time	Phase Composition			
	YbDS %	YbMS %	Al_2O_3 %	YbAG %
20 Hours	69.8	30.2	N/D	N/D
40 Hours	52.3	47.3	N/D	N/D

Steam Exposure Time	Phase Composition			
	YbDS %	YbMS %	Al_2O_3 %	YbAG %
20 Hours	96.5	N/D	N/D	3.5
40 Hours	95.2	N/D	N/D	4.8

Fig. 3. X-Ray diffraction patterns and surface phase ratios of (a) YbDS and (b) YbDS/3Al_2O_3 after 20 h (red profile) and 40 h (black profile) of steam exposure at 1350 °C; showing formation of YbMS on the Al_2O_3 free specimen and the hindering effect of Al_2O_3 on transformation of YbDS to YbMS. The peak positions for YbDS, YbMS, YbAG and Al_2O_3 are based on the reference diffraction data displayed below the XRD patterns of specimens. N/D: Not detected.

intensities increased with exposure duration. The Rietveld refinements showed that the YbMS phase ratio on the surface increased from approximately 30–47% after steam exposure from 20 h to 40 h, as expected. In contrast, no evidence of YbMS diffraction peaks was found in the XRD patterns obtained for the YbDS/3Al_2O_3 (Fig. 3-b). While the intensity of the Al_2O_3 peaks decreased after steam exposure, the peaks corresponding to the YbAG increased in intensity. Based on the Rietveld refinements of XRD results, the phase ratio for YbAG became 3.5% and 4.8% after 20 and 40 h of steam exposure, respectively. These results indicate that the addition of 3 wt% Al_2O_3 was able to enough to promote the formation of YbAG phase hindering the water vapour degradation of YbDS into YbMS and $Si(OH)_4$.

3.2.2. *Surface microstructure evolution*

SEM micrographs of the YbDS and YbDS/3Al_2O_3 surfaces, obtained after 20 h and 40 h of steam exposure are shown in Fig. 4. In comparison to the as-sintered surface (Fig. 2-a), the majority of the Al_2O_3 free specimen's surface had transformed to a porous second phase with refined grain morphology after 20 h of steam exposure (Fig. 4-a). This new composition was confirmed to be YbMS according to the EDS analysis conducted on Spot 1. However, some YbDS grains were still present at the surface, as demonstrated by EDS Spot 2 (Table 3). After 40 h of steam exposure, YbMS was the only phase observed on the surface of Al_2O_3 free specimens (EDS Spot 3). In addition, steam exposure also led to surface cracking as highlighted in Fig. 4-a and b, and an increase in porosity from 7 vol% to 15 vol%.

For the YbDS/3Al_2O_3 specimen, evidence of grain refinement was observed (Fig. 4-c, and d) without the presence of apparent porosity as previously observed with the YbDS specimen. Nevertheless, some surface pores were detected after 40 h of steam exposure (highlighted with arrow and circle in Fig. 4-d). These areas may correspond to sites of residual Al_2O_3 grains that are consumed during steam corrosion test, because no surface pores were observed on the as-sintered specimens. On the other hand, the EDS analysis shows the steam exposed composite specimens had the same composition as the as-sintered state (EDS Spots 3, 4, 5 and 6 in Table 2 and 5, 6, 7 and 8 in Table 3). According to Castaing's formula [19], EDS analysis with SEM may be insufficient to determine the composition of a surface layer of sub-micron thickness due to the penetration depth of the X-rays.

$$Z_m = 0.033\left(E_0^{1.7} - E_c^{1.7}\right)\frac{A}{\rho Z} \quad (3)$$

Where, Z_m is the penetration depth of the X-Rays generated by EDS detector, E_0 and E_c are the accelerating voltage and minimum emission voltages (keV) respectively, A is the atomic mass, ρ is the density (g/cm^3) and Z is the atomic number. With the parameters used in EDS analysis, a minimum penetration depth for the possible phases (i.e. YbDS, YbMS, YbAG or Al_2O_3) was calculated to be approximately 460 nm. This result suggests that any elemental changes at the surface of the YbDS/3Al_2O_3 cannot be detected with EDS analysis if a surface much thinner than 460 nm was formed.

Mass loss has been measured for both YbDS and YbDS/3Al_2O_3 specimens after the steam for 40 h. The mass loss of YbDS has been found to be 12.6 mg/cm^2 which could be due to removal of silica and formation YbMS, whereas for the YbDS/3Al_2O_3 sample there was no mass change.

3.2.3. *Cross-sectional microstructure analysis using SEM and TEM*

Fig. 5 shows the polished cross-sections of the YbDS and YbDS/3Al_2O_3 specimens after 20 and 40 h of steam exposure. Fig. 5-a revealed the formation of a continuous and porous YbMS layer after 20 h with an average equivalent thickness of 0.8 ± 0.3 μm in the Al_2O_3 free specimens; effectively replacing the YbDS on the outermost layer of the specimen. Extending the exposure time to 40 h, the YbMS layer increased the thickness to 1.8 ± 0.5 μm (Fig. 5-b). It should also be noted that the thickness of the newly formed YbMS layer on YbDS was much lower than the penetration depths of X-rays for performing XRD (measured to be in the range of 15 μm for Yb based silicates). As such, YbDS peaks were also detected on the XRD patterns of this specimen after steam corrosion test. In contrast, the YbDS/3Al_2O_3 specimen did not show any discernible outer YbMS layer even after 40 h of steam exposure as shown in Fig. 5-c and d. These results were found to be in accordance with the XRD and surface SEM analysis, suggesting an enhanced steam corrosion resistance of YbDS/3Al_2O_3 composite specimen in comparison to YbDS.

No significant phase change was detected on the YbDS/3Al_2O_3 sample after steam exposure according to the XRD and EDS analysis conducted on the surface, despite obvious microstructural evolution. In

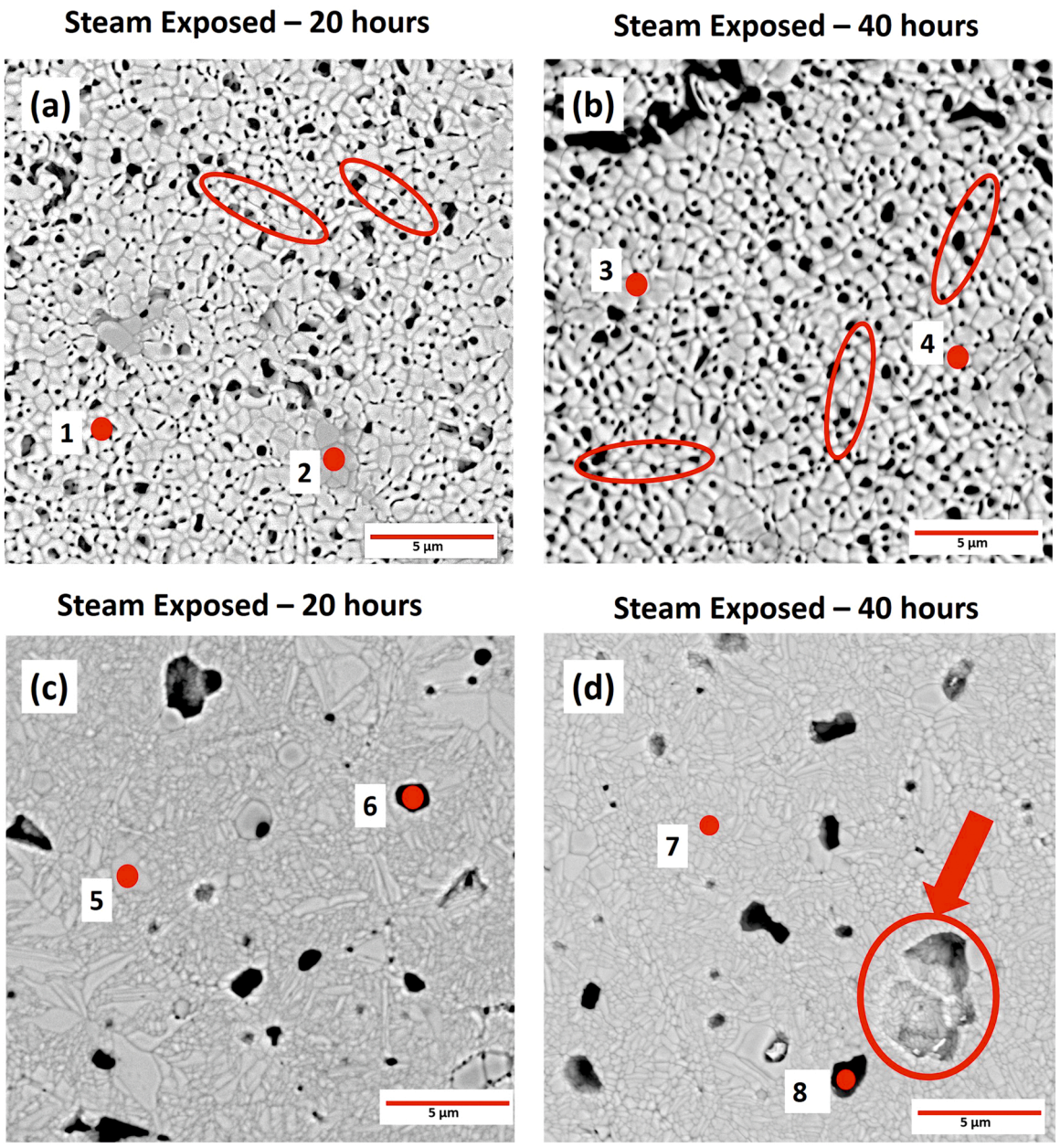

Fig. 4. (a), (b) are surface microstructures of YbDS after 20 h and 40 h of steam exposure respectively, showing the phase transformation to YbMS together with porosity increase and crack generation with longer exposure. (c), and (d) are the surface micrographs of YbDS/3Al_2O_3 after 20 h and 40 h of steam exposure respectively. Micrographs show grain refinement with increasing exposure time and pore formation (highlighted with red circle). EDS analysis of the marked eight spots on each figure are given in Table 3.

Table 3
Summary of the compositional data for the spot marked in the micrographs of YbDS and YbDS/3Al_2O_3 (Fig. 4) after steam exposure.

	Elemental Composition (at%)				Corresponding Phase		Elemental Composition (at%)				Corresponding Phase
Spot#	O	Yb	Si	Al		Spot#	O	Yb	Si	Al	
1	61	25.2	13.8	N/D	YbMS	5	60	20.9	19.1	N/D	YbDS
2	63.9	18.1	18	N/D	YbDS	6	60.2	N/D	N/D	39.8	Al_2O_3
3	63.1	24.3	12.6	N/D	YbMS	7	58	19.9	18.1	N/D	YbDS
4	62.7	24.9	12.4	N/D	YbMS	8	59.2	N/D	N/D	40.8	Al_2O_3

N/D: Not detected

order to identify whether a thin corrosion protective layer formed on the surface, a cross-sectional lamella was prepared via FIB to conduct TEM analysis.

In the high-angle annular bright-field image (HAABF) presented in Fig. 6-a, the YbDS grains underneath the surface still have a similar grain size (GS>10 µm) to the YbDS prior to steam exposure (Fig. 2-c). In addition, a dense layer formed over the YbDS grains across the entire surface of the TEM lamellae (Fig. 6-b and c). The thickness of the layer

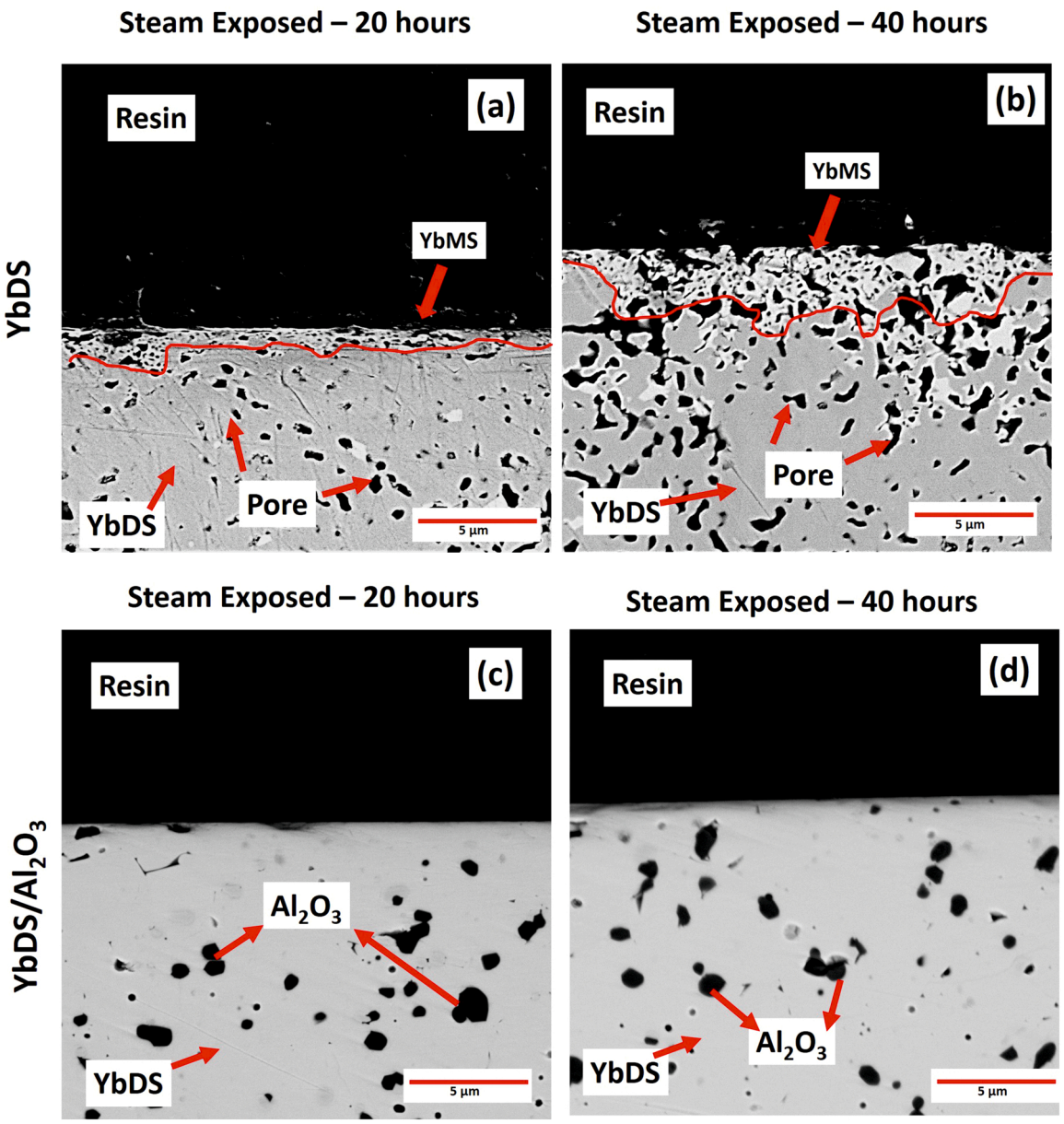

Fig. 5. Polished cross-sectional SEM micrographs after steam exposure: YbDS (a) for 20 h, (b) for 40 h and YbDS/3Al_2O_3 (c) for 20 h and (d) for 40 h. Increasing thickness of YbMS was observed for the YbDS, but no reaction layer formed on the surface of YbDS/Al_2O_3.

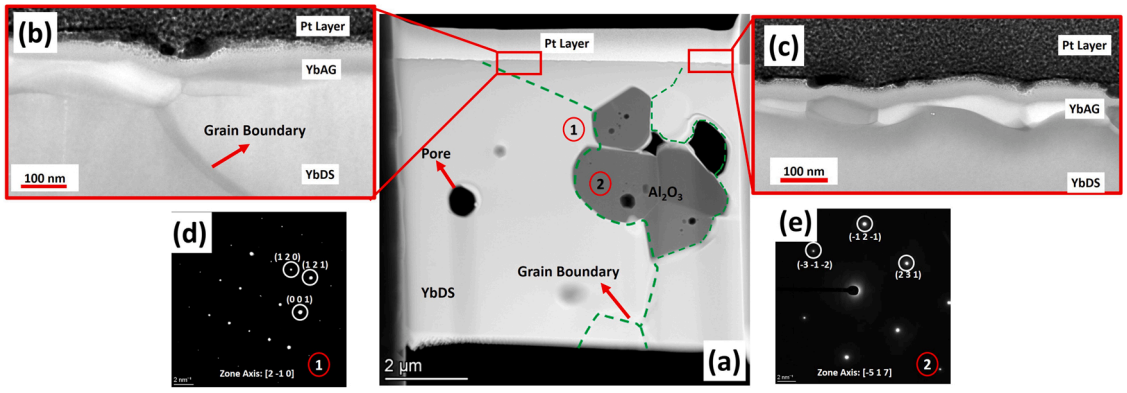

Fig. 6. (a) TEM lamellae of YbDS/3Al_2O_3 milled by FIB after 20 h of steam exposure; showing coarse grains of YbDS, and a second phase of darker contrast. (b) magnified HAABF/STEM image shows a continuous layer on the surface, (c) and (d) SAD patterns of Area-1 for YbDS and Area-2 for Al_2O_3.

varied significantly across the surface, ranging from 80 nm in the areas closer to the grain boundary of YbDS to 110 nm on the surface of the YbDS grains. Fig. 6-d and e show the diffraction patterns of Areas-1 and 2 in Fig. 6-a. Area-1 was indexed as C/2 m YbDS whereas Area-2 was indexed as R-3c Al_2O_3. These observations provide conclusive evidence that a new phase formed on the surface of YbDS/3Al_2O_3 after steam exposure and confirms that YbDS and residual Al_2O_3 had the same morphology after initial sintering and steam exposure.

Unfortunately, the thickness of the outer layer was insufficient to conduct diffraction analysis on, therefore EDS was used to investigate its composition. Fig. 7-a shows elemental EDS mapping results of the surface layer formed after steam exposure. It is apparent that the layer was rich in ytterbium, aluminium and oxygen but low in silicon. In order to quantify any atomic fraction change through the layer, an EDS line scan was also conducted. The profile (marked on Fig. 7-a) and the average fractions of ytterbium, aluminium, oxygen and silicon are given in Fig. 7-b and c respectively. The composition was found to be consistent with YbAG (Yb:Al:O – 15:25:60). Therefore, the formation of a YbAG layer on the surface, protected the YbDS against corrosion in the water vapour environment.

3.2.4. *Evolution of the microstructure of YbDS/3Al_2O_3 after short term high temperature steam exposure*

In order to determine the formation mechanism of the YbAG layer, the polished surfaces of as-sintered YbDS/3Al_2O_3 were exposed steam for 20 min and 40 min. Fig. 8 shows SEM micrographs of the composite specimen surface after these different exposure times. The results revealed that the formation of YbAG initiated at residual Al_2O_3 grains that likely acted as sources of Al^{3+} ions (Fig. 8-a). When the exposure time extended from 20 to 40 min, the area of YbAG phase enlarged and individual YbAG grains could be seen coalescing to form a continuous layer (Fig. 8-b). This observation provides a supporting evidence in favour of surface diffusion being the primary mechanism responsible for the formation of YbAG. Assuming that the YbAG layer is formed through surface diffusion, the diffusion coefficient has been estimated as $\sim 10^{-9}$ cm^2/s based on the area covered by the YbAG and elapsed exposure time. These results suggest that the surface of the YbDS/3Al_2O_3 most likely covered in very early stages of the steam corrosion test that lasted for 20 h and 40 h. It should also be noted that the YbAG phase formed through the diffusion process has much smaller grains than that of YbDS.

Fig. 9 shows a high-angle annular dark-field (HAADF)/STEM image of the YbDS/3Al_2O_3 cross-section after 40 min of steam exposure with EDS elemental maps performed in selected areas. The overview STEM image displayed in the middle of Fig. 9 contained two phases; (i) Al_2O_3 appeared in darker contrast on the surface, (ii) YbDS appeared in brighter contrast. The EDS analysis at higher magnification areas showed aluminium enrichment and silicon depletion in the surface layer in close to the Al_2O_3 grain (Fig. 9-a, and b). However, the thickness of this surface layer decreased with increasing distance from the Al_2O_3 grain (Fig. 9-c). Furthermore, the layer was no longer present at the other side of the grain boundary (Fig. 9-d and e).

These results are consistent with the surface SEM micrographs, displayed in Fig. 8, and provide further support for the hypothesis that surface diffusion of aluminium from the residual Al_2O_3 grain was the main mechanism for the formation of the YbAG layer. In addition, the surface level of the Al_2O_3 grain was lower than YbDS although the specimen was polished prior to the steam corrosion test. This discrepancy could be attributed the consumption of Al_2O_3 during the steam

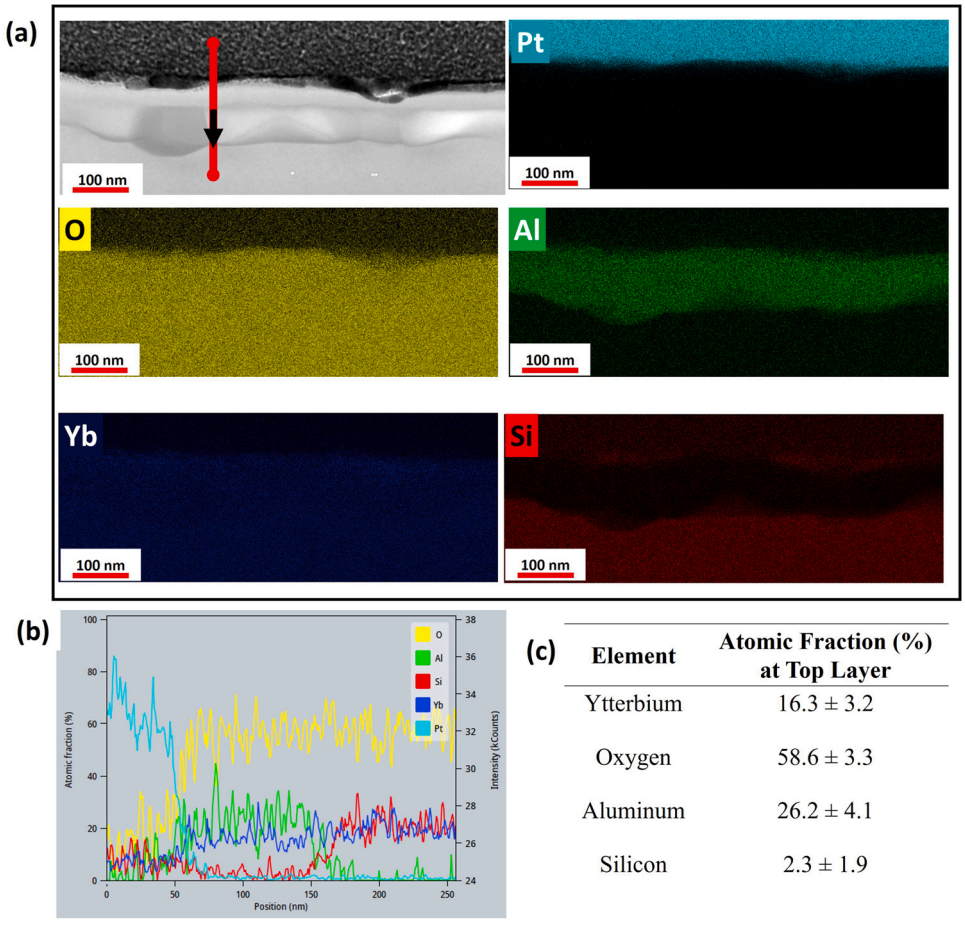

(c)

Element	Atomic Fraction (%) at Top Layer
Ytterbium	16.3 ± 3.2
Oxygen	58.6 ± 3.3
Aluminum	26.2 ± 4.1
Silicon	2.3 ± 1.9

Fig. 7. TEM compositional analysis of YbDS/3Al_2O_3; (a) EDS mapping, (b) line scan profile through the layer marked on (a), (c) atomic fraction of elements in top layer; confirming the YbAG layer formation.

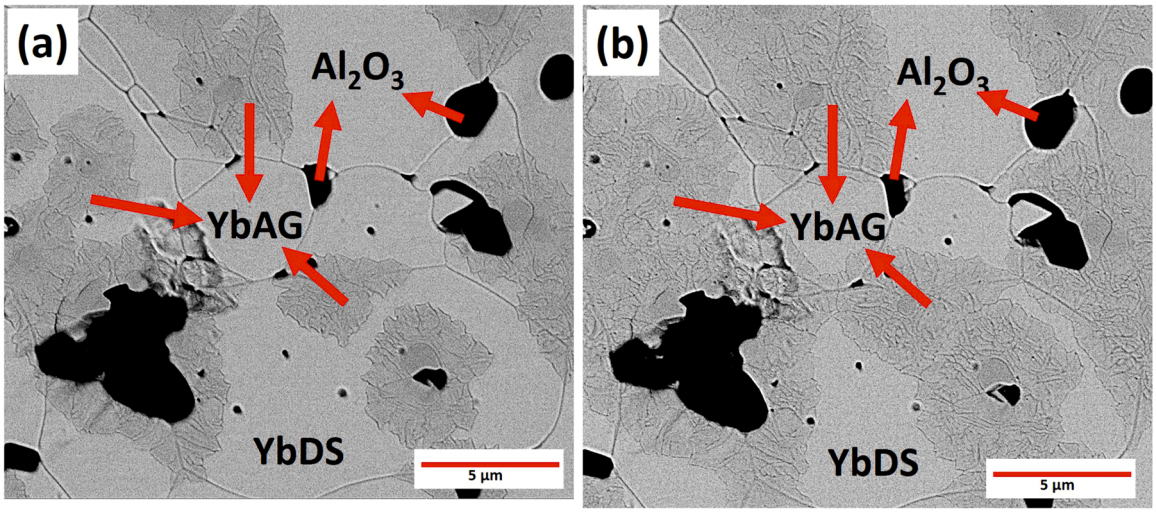

Fig. 8. SEM micrograph of YbDS/3Al_2O_3 after steam exposure for (a) 20 min and (b) 40 min at 1350 °C; showing formation of YbAG phase via surface diffusion from the residual Al_2O_3 grains.

exposure as the aluminium diffuses to the steam exposed surface of YbDS.

4. Discussion

4.1. Effect of the Al_2O_3 addition on the sintering behaviour of YbDS

Comparison of the microstructures of the YbDS and Al_2O_3 containing YbDS specimens showed the beneficial effect of Al_2O_3 on sintering behaviour. The addition of Al_2O_3 enabled to obtain fully dense microstructure and also resulted in significant grain growth in YbDS with an average grain size of 13.6 µm, whereas the average grain size of the Al_2O_3 free specimen was 0.8 µm. It has been shown by Lee et al. [20] that YbDS-Al_2O_3 system has a eutectic temperature of 1459 °C, only 9 °C higher than that of the sintering temperature used in this study. Moreover, based on the ternary phase diagram of Yb_2O_3 – SiO_2 – Al_2O_3, the formation of a liquid and/or a viscous phase is very likely during sintering along with a new YbAG phase, which is the reaction product of YbDS and Al_2O_3 according to the reaction given in Eq.2 [12]. The grain morphologies (i.e. facetted grains with round corners) of composite specimens shown in Fig. 2-b, c and d suggest that liquid phases may be present during the initial sintering at 1450 °C, as similar grain morphologies are seen with liquid phase sintering for various material systems [21].

4.2. Formation of YbAG protective surface layer

The most obvious finding to emerge from the analysis of YbDS/3Al_2O_3 is that, the formation of YbAG as a thin surface layer was only observed in the presence of steam. Therefore, it is proposed that Eq.5 describes the YbDS/3Al_2O_3 interaction with steam.

$$3Yb_2Si_2O_{7\,(s)} + 5Al_2O_{3\,(s)} + 12\,H_2O_{(g)} \rightarrow 2Yb_3Al_5O_{12} + 6Si(OH)_{4\,(g)} \quad (5)$$

No formation of the YbAG layer was observed at the surface of YbDS/3Al_2O_3 after sintering in air, which suggests the reaction between YbDS and Al_2O_3 in air (given in Eq.2) is much slower than reaction in Eq.5. This slow reaction rate also appears to be the reason of residual Al_2O_3 grains observed on the surface of as-sintered specimen (Fig. 2-b,c and d).

From the results shown in Figs. 4 to 9, a schematic describing the formation of YbAG layer on the surface of Al_2O_3 containing YbDS specimen is given in Fig. 10. The primary interaction mechanism between YbDS and Al_2O_3 forming YbAG is proposed to be a result of water vapour molecules reacting with silicon-oxygen polyhedral (SiO_4) of YbDS to form $Si(OH)_4$. Meanwhile Al^{3+} ions replace the Si^{4+} in YbDS via surface diffusion from residual Al_2O_3 grains to form a YbAG layer until the surface of YbDS is completely covered or the Al_2O_3 grains adjacent to the surface are fully consumed (Fig. 4-d).

YbDS has a monoclinic structure with the c/2 m space group. It is comprised of a YbO_6 octahedron sharing corners with six equivalent SiO_4 tetrahedrons. In a theoretical study about the formation and diffusion of point defects in ytterbium silicates, it has been reported that YbDS accommodates oxygen vacancies around the SiO_4 tetrahedron and there are five possible path vacancy to migrate through [22]. Wada et al. [23] studied the water vapour mass transfer in YbDS and found that the oxygen permeation of YbDS is mainly controlled by diffusion of OH^- and O^{2-} ions. They also reported that, even under dry conditions, oxygen can diffuse through vacancies in YbDS, but it is the water vapour reacts with the SiO_2 to form $Si(OH)_4$ and result in the transformation of YbDS to YbMS (Eq.1).

Table 4 shows previously reported energies and the bond lengths between Yb-O, Si-O and Al-O in different polyhedrons. It is notable that the bonding energies in polyhedrons of YbAG are considerably higher than those in polyhedrons of YbDS or YbMS. In addition, the lengths of the Al-O bond are much shorter than the Si-O bond present in YbDS or YbMS, indicating that during the formation of YbAG from YbDS and Al_2O_3 in the environment of water vapour, much stronger bonds are formed. This strong bonding nature of YbAG may explain its greater phase stability than YbMS and also the energetic favourability of forming YbAG compared to YbMS.

The protective nature of the YbAG observed in this study is consistent with previous studies. Klemm et al. [25] studied the water vapour corrosion behaviour of several materials including YbDS and YbAG, and reported that YbAG had a corrosion rate three times lower than YbDS. This can be associated with the strong bonding of aluminium compound and less oxygen vacancy concentration in YbAG compare to weaker bonding silicon compound and higher vacancy concentration in YbDS.

4.3. Thermodynamics of reactions

Table A1 details previously reported room temperature formation enthalpies of YbMS, YbDS and YbAG. The formation of YbAG with − 6987.9 kJ/mole [26], is the most exothermic in comparison to the formation enthalpies of YbDS and YbMS reported as, − 3523.7 kJ/mole [27] and − 2774.7 kJ/mole [27] respectively. These values indicate the higher phase stability of YbAG than that of silicate based compounds. In order to associate thermodynamic favourability of the reactions

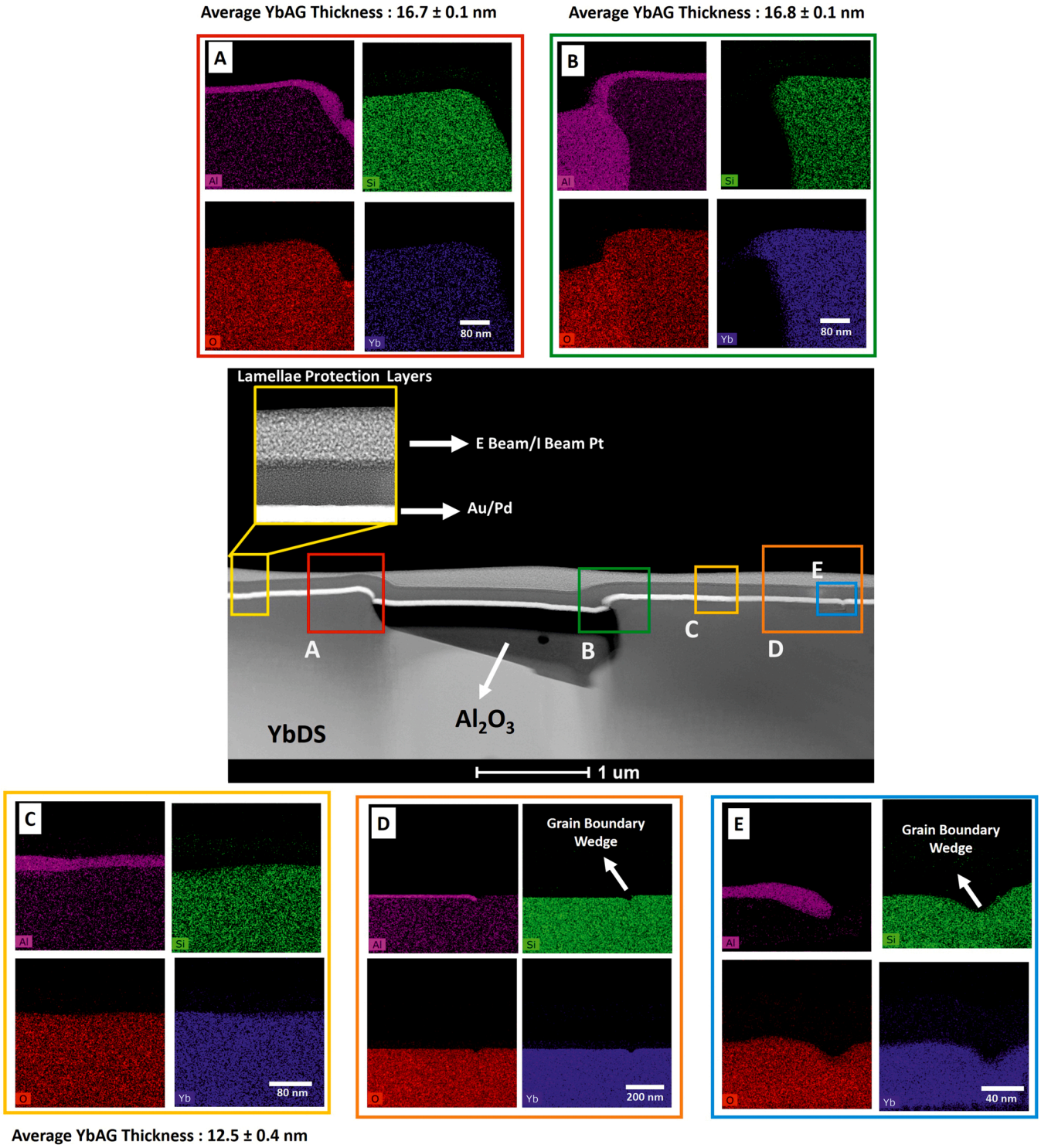

Fig. 9. HAADF/STEM image of the YbDS/3Al_2O_3 specimen after steam exposure for 40 min at 1350 °C showing the surface microstructure, (a), (b), (c), (d) and (e) are EDS elemental maps of the marked areas on the HAADF/STEM image, showing formation of YbAG layer via surface diffusion from Al_2O_3 grain.

occurring between YbDS and Al_2O_3, and steam, reaction Gibbs free energies for standard state conditions (298 K, 1 atm) were calculated according to the Eqs. 6 and 7 (Table 5).

$$\Delta G^0_{rxn} = \Delta G^0_{Products} - \Delta G^0_{Reactants} \quad (6)$$

$$\Delta G^0_{rxn} = \Delta H^0_{rxn} - T\Delta S^0_{rxn} \quad (7)$$

Where ΔG^0 is standard-state free energy, ΔH^0 and ΔS^0 are the enthalpy and entropy changes respectively, and T is the temperature (K).

For standard conditions, the molar Gibbs free energy of the YbDS to YbMS reaction in steam environment (Reaction (1) in Table 5) was found as; − 1.3 kJ.mol^{-1}. On the contrary, the Gibbs free energy of reaction between YbDS and Al_2O_3 in steam was determined as (Reaction (2) in Table 5); 77.9 kJ.mol^{-1}. From these calculations, it would be expected that the first reaction is more favourable which conflict with the observations in this study as the formation of YbAG was very obvious

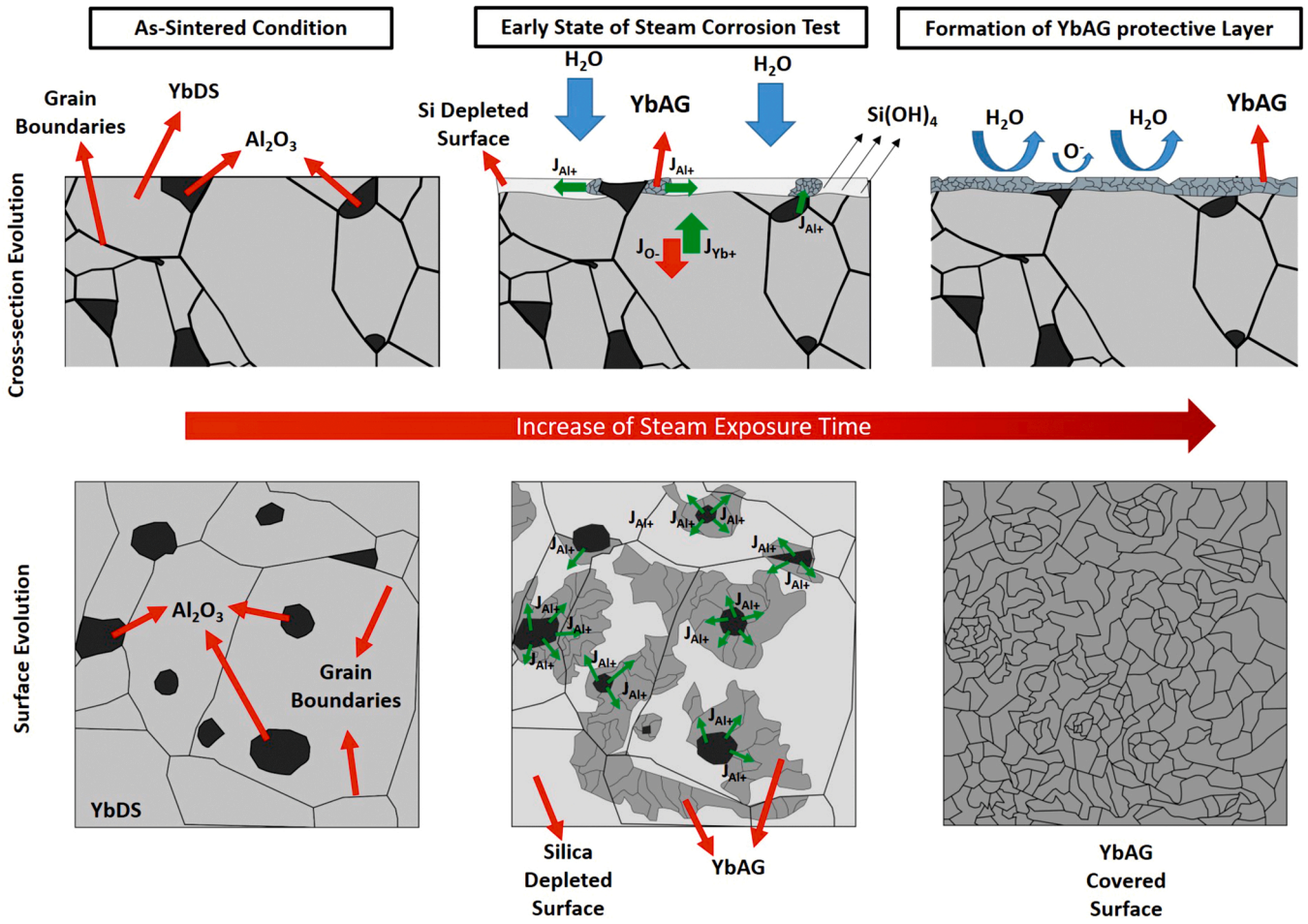

Fig. 10. Formation mechanism of YbAG on surface of Al_2O_3 containing composite via surface diffusion; (a) cross-sectional overview, (b) surface overview.

Table 4
Estimated bond energies and bond lengths in various polyhedral and corresponding compounds.

	Energy Range (kJ/mol)	Bond Length (A)	Polyhedra	Compound
Yb-O[a]	1156–2336	2.26 ± 0.03	YbO_6	YbDS/YbMS
Yb-O[a]	851–979	2.33 ± 0.12	YbO_7	YbMS
Yb-O[b]	8974–9387	2.30	YbO_8	YbAG
Si-O[a]	3845–4287	1.64 ± 0.01	SiO_4	YbDS/YbMS
Al-O[b]	28,001	1.88	AlO_4	YbAG
Al-O[b]	15,708	1.72	AlO_6	YbAG

[a] Xiang et al. [24],
[b] Zhou et al. [13]

in microstructural examinations. However, these calculations do not take into account the conditions of testing environment of the present study. Hence, the Gibbs free energies for Reactions (1) and (2) in Table 5 should be calculated according to Eqs. 8 and 9 considering partial pressure of $Si(OH)_{4(g)}$ and $H_2O_{(g)}$, which determines the direction of Reaction (1) and (2) in Table 5. The partial pressure ratio, K, in Eq. 9 is expected to much smaller than 1, due to the gradual formation of $Si(OH)_{4(g)}$ which is then removed from the furnace chamber by steam flow [15,28,29].

$$\Delta G = \Delta G^0_{rxn} + RTlnK \quad (8)$$

Table 5
Standard State reaction enthalpies and Gibbs free energies at the temperature of steam corrosion test (T: 1623 K).

Reaction	ΔH^0_{rxn} (1623 K) (kJmol^{-1})	ΔG^0_{rxn} (1623 K) (kJmol^{-1})
(1) $Yb_2Si_2O_{7(s1623K)} + 2\ H_2O_{(g,1623\ K)} \rightarrow Yb_2SiO_{5(s,1623\ K)} + Si(OH)_{4(g,1623\ K)}$	-101.5	-1.3
(2) $1/2\ Yb_2Si_2O_{7(s,1623\ K)} + 5/6\ Al_2O_{3(s,1623\ K)} + 2\ H_2O_{(g,1623\ K)} \rightarrow 1/3\ Yb_3Al_5O_{12(s,1623\ K)} + Si(OH)_{4\ (g,1623\ K)}$	-35.4	92.9
(3) $Yb_2SiO_{5(s,1623\ K)} + 5/3\ Al_2O_{3(s,1623\ K)} + 2\ H_2O_{(g,1623\ K)} \rightarrow 2/3\ Yb_3Al_5O_{12(s,1623\ K)} + Si(OH)_{4\ (g,1623\ K)}$	30.6	187.1
(4) $Yb_2Si_2O_{7(s,1623\ K)} + 5/3\ Al_2O_{3(s,1623\ K)} \rightarrow 2/3\ Yb_3Al_5O_{12} + 2\ SiO_{2(s,1623\ K)}$	-188.3	-135.7

[a, b] Reaction enthalpies of YbDS and YbMS were calculated using the Neumann-Kopp method and their heat capacities derived from their binary oxides (Yb_2O_3 and SiO_2) using [30] (see Appendix). [c] Reaction enthalpy of YbAG was calculated using heat capacity value reported by Wang et al. [31].

Where, ΔG is free energy at any moment, R is the gas constant T is temperature (K), K is the ratios of the partial pressures for chemical equilibrium condition. For the Reactions (1) and (2) in Table 5, K can be written as follow;

$$K = \frac{P_{Si(OH)_4}}{(P_{H_2O})^2} \quad (9)$$

Where two molecules of $H_2O_{(g)}$ are needed to form one molecule of $Si(OH)_{4(g)}$.

Assuming a negative Gibb's free energy makes Reaction (2) favourable, the K value should be smaller than 1.02×10^{-3}. This result indicates that the partial pressure of $Si(OH)_{4(g)}$ in steam corrosion test was much smaller than $H_2O_{(g)}$, and the gas velocity used in the current study was sufficient enough to drive both reactions (Reaction (1) and Reaction (2) in Table 5) to form $Si(OH)_4$. However, the observation of residual Al_2O_3 on the surface of the composite specimen, suggest that Reaction (2) in Table 5 is more dominant than Reaction (1). This indicates that the surface diffusion of aluminium to silica depleted YbDS is fast enough to form YbAG according to the Reaction (2) in Table 5.

Under the conditions of testing environment (i.e. where the partial pressure difference influences the reaction), another possible reaction path is the formation of YbMS first (Reaction (1) in Table 5) and then the sequential reaction of YbMS with Al_2O_3 (Reaction (3) in Table 5) to form YbAG. However, the calculated reaction enthalpy and standard state Gibbs free energy shows that Reaction (3) is less favourable in comparison to the direct reaction of YbDS with Al_2O_3 to form YbAG in steam (Reaction (2) in Table 5). Moreover, as displayed in Fig. 4-a and b, the reaction of YbDS to YbMS (Reaction (1) in Table 5), results in significant surface porosity, and the lack of this in steam exposed surface of YbDS/$3Al_2O_3$ (Fig. 8) confirms that the formation of YbAG from YbMS (Reaction (1) and (3)) is unlikely, in comparison to Reaction (2).

The Gibbs free energy calculations also indicate that Reaction (4) in Table 5 should be thermodynamically favourable; however, at the temperature of the water vapour corrosion test (1350 °C) solid state diffusion appears to limit the formation of YbAG below the surface where water vapour is absent.

5. Conclusion

In this study the effects of Al_2O_3 addition to YbDS on sintering, and steam corrosion behaviour at 1350 °C are studied. The following conclusions can be drawn;.

1. The addition of Al_2O_3 as a sintering agent increased the relative density of the specimen and resulted in significant grain growth due to liquid/viscous phase sintering occurring during initial sintering at 1450 °C.
2. The formation of ytterbium alumina garnet ($Yb_3Al_5O_{13}$-YbAG) has been observed, in the 3 wt% Al_2O_3 containing specimen, however residual (non-reacted) Al_2O_3 was also present and has been confirmed by SEM and XRD analysis.
3. YbDS specimens suffered surface recession during water vapour exposure due to the depletion of the silica phase, which led to the formation of a porous YbMS layer. The thickness of the YbMS corrosion layer increased with the water vapour exposure time.
4. No coating recession or YbMS phase were observed even after 40 h of steam exposure of YbDS/$3Al_2O_3$ due to the formation of a protective YbAG layer on the surface via surface diffusion from residual Al_2O_3 grains that were present in the as-sintered state.
5. The reaction of YbDS, Al_2O_3 and steam was controlled by the partial pressure differences between the gaseous compounds (i.e. $Si(OH)_4$ and H_2O). It was also a reason for the faster formation of YbAG in water vapour.
6. Results from this study indicate a possible method of developing improved EBCs through greater resistance to steam corrosion. However, given the limited studies undertaken to date, further research should investigate the long term protection of YbAG surface layer.

CRediT authorship contribution statement

Ahmet Hilmi Paksoy: Conceptualization, Methodology, Investigation, Visualization, Writing – original draft, Writing – review & editing. **Joao P. Martins:** Investigation, Writing - review & editing. **Huatang Cao:** Investigation. **Ying Chen:** Investigation. **Grant Gibson:** Writing – review & editing. **Ping Xiao:** Supervision, Writing – review & editing, Project administration, Funding acquisition.

Declaration of Competing Interest

The authors declare that they have no known competing financial interests or personal relationships that could have appeared to influence the work reported in this paper.

Data availability

Data supporting the figures and findings of this manuscript are available from the corresponding authors upon reasonable request.

Acknowledgements

The authors thank Simon McCormack, Esma Yilmaz and Daniel Scotson of University of Manchester for their helpful discussions. Ahmet Hilmi Paksoy acknowledges funding support from The Scientific and Technological Research Council of Turkey (TUBITAK) and Rolls-Royce for his Ph.D. study. Ping Xiao would like to acknowledge support from the Royal Academy of Engineering and Rolls-Royce for the appointment of Rolls-Royce/Royal Academy of Engineering Research Chair in Advanced Coating Technology.

Appendix

See Appendix Table A1.

Table A1 shows thermodynamic data used in the current study to evaluate Gibbs free energies of the proposed reactions of YbDS with water vapour and Al_2O_3. The formation enthalpies and entropies of the solid and gas compounds at room temperature were used as a reference. Furthermore, enthalpy and entropy values at the steam exposure temperature (1350 °C) were calculated using the change of heat capacities with temperature. However, YbDS, YbMS and YbAG, only the heat capacity (C_p) data of YbAG is available in the literature [31]. Therefore, to modify the enthalpies to the conditions of the steam corrosion test, the dependence of the heat capacities with temperature for YbDS and YbMS were estimated using the Neumann-Kopp rule (NKR), which is a reliable method for complex oxide compounds [30].

Table A1
Thermodynamic properties used in the calculations.

Compound	ΔH_f (298 K) (kJ.mol^{-1})	S° (298 K) (kJ.mol^{-1})
(1) $Yb_2O_{3(s)}$[a]	-1814.6	133
(2) $SiO_{2(s)}$[a]	-910	41.4
(3) $Al_2O_{3(s)}$[a]	-1675.7	50.9
(4) $H_2O_{(g)}$[a]	-241.8	188.5
(5) $Si(OH)_{4(g)}$[b]	-1340.6	347.7
(6) $Yb_2SiO_{5(s)}$	-2774.7[c]	174.5[d]
(7) $Yb_2Si_2O_{7(s)}$	-3523.7[c]	216[d]
(8) $Yb_3Al_5O_{12(s)}$	-6987.9[e]	312[e]
C_p^0 (Yb_2O_3)[a]: 136–2.017 × 10^{-3} T – 1.9928 × 10^6 T^{-2}		
C_p^0 (SiO_2 α- Quartz, 298–844 K)[a] = 44.6 + 3.78 × 10^{-2} T – 10^6 T^{-2}		
C_p^0 (SiO_2 β-Quartz, 844–1800 K)[a] = 58.9 + 10^{-2} T		
ΔH (α to β, 844 K)[a] = 0.625 kJ.mol^{-1}		
C_p^0 (Al_2O_3)[a]: 157 + 7.19 × 10^{-4} T - 9.88 × 10^2 $T^{-0.5}$ - 1.90 × 10^5 T^{-2}		
C_p^0 (H_2O)[a]: 7.36 + 2.74 × 10^{-2} T - 4.81 × 10^{-6} T^2 + 3.62 × 10^2 $T^{-0.5}$ - 2.23 × 10^5 T^{-2}		
C_p^0 ($Si(OH)_4$)[b]: 139.722 + 1.98 × 10^{-2} T - 2.76 × 10^6 T^{-2}		
C_p^0 (Yb_2SiO_5)[c]: 194 + 2.75 × 10^{-2} T - 6.08		
C_p^0 ($Yb_2Si_2O_7$)[c]: 2.71–2.48 × 10^{-2} T - 9.56 × 10^6 T^{-2}		
C_p^0 ($Yb_3Al_5O_{12}$)[d]: 466 + 3.38 × 10^{-2} T - 1.04 × 10^6 T^{-2}		

[f]Estimated using Neumann-Kopp rule (NKR)
[a] Robie et al. [32],
[b] Plyasunov et al. [33],
[c] Ogawa et al. [27],
[d] Estimated from binary oxides (Yb_2O_3 and Al_2O_3)
[e] Glasser et al. [26]

References

[1] R. Naslain, Design, preparation and properties of non-oxide CMCs for application in engines and nuclear reactors: an overview, Compos. Sci. Technol. 64 (2004) 155–170, https://doi.org/10.1016/S0266-3538(03)00230-6.
[2] S. Schmidt, S. Beyer, H. Knabe, H. Immich, R. Meistring, A. Gessler, Advanced ceramic matrix composite materials for current and future propulsion technology applications, Acta Astronaut. 55 (2004) 409–420, https://doi.org/10.1016/j.actaastro.2004.05.052.
[3] J.L. Smialek, R.C. Robinson, E.J. Opila, D.S. Fox, N.S. Jacobson, SiC and Si3N4 recession due to SiO2 scale volatility under combustor conditions, Adv. Compos. Mater. 8 (1999) 33–45, https://doi.org/10.1163/156855199×00056.
[4] E.J. Opila, Oxidation and volatilization of silica formers in water vapor, J. Am. Ceram. Soc. 86 (2003) 1238–1248, https://doi.org/10.1111/j.1151-2916.2003.tb03459.x.
[5] Y.-C. Zhou, C. Zhao, F. Wang, Y.-J. Sun, L.-Y. Zheng, X.-H. Wang, Theoretical prediction and experimental investigation on the thermal and mechanical properties of bulk β-$Yb_2Si_2O_7$, J. Am. Ceram. Soc. 96 (2013) 3891–3900, https://doi.org/10.1111/jace.12618.
[6] S. Ueno, T. Ohji, H.T. Lin, Recession behavior of Yb2Si2O7 phase under high speed steam jet at high temperatures, Corros. Sci. 50 (2008) 178–182, https://doi.org/10.1016/j.corsci.2007.06.014.
[7] E. Bakan, M. Kindelmann, W. Kunz, H. Klemm, R. Vaßen, High-velocity water vapor corrosion of Yb-silicate: sprayed vs. sintered body, Scr. Mater. 178 (2020) 468–471, https://doi.org/10.1016/j.scriptamat.2019.12.019.
[8] B.T. Richards, K.A. Young, F. De Francqueville, S. Sehr, M.R. Begley, H.N. G. Wadley, Response of ytterbium disilicate-silicon environmental barrier coatings to thermal cycling in water vapor, Acta Mater. 106 (2016) 1–14, https://doi.org/10.1016/j.actamat.2015.12.053.
[9] N. Rohbeck, P. Morrell, P. Xiao, Degradation of ytterbium disilicate environmental barrier coatings in high temperature steam atmosphere, J. Eur. Ceram. Soc. 39 (2019) 3153–3163, https://doi.org/10.1016/j.jeurceramsoc.2019.04.034.
[10] Y. Lu, L. Luo, J. Liu, C. Zhu, Y. Wang, N. Jacobson, Failure mechanism associated with the thermally grown silica scale in environmental barrier coated C/SiC composites, J. Am. Ceram. Soc. 99 (2016) 2713–2719, https://doi.org/10.1111/JACE.14273.
[11] K.N. Lee, Yb2Si2O7 Environmental barrier coatings with reduced bond coat oxidation rates via chemical modifications for long life, J. Am. Ceram. Soc. 102 (2019) 1507–1521, https://doi.org/10.1111/JACE.15978.
[12] Y. Murukami, H. Yamamoto, Phase equilibria and properties of glasses in the alumina-ytterbia-silica system, J. Ceram. Soc. Jpn. 1106 (1993) 1101–1106.
[13] Y. Zhou, H. Xiang, Z. Feng, Theoretical investigation on mechanical and thermal properties of a promising thermal barrier material: Yb3Al5O12, J. Mater. Sci. Technol. 30 (2014) 631–638, https://doi.org/10.1016/j.jmst.2014.06.007.
[14] H. Klemm, F. Marco, Corrosion of ceramic materials in hot gas environment, 28th Int. Conf. Adv. Ceram. Composites B (2004) 167–172.
[15] N. Maier, K.G. Nickel, G. Rixecker, High temperature water vapour corrosion of rare earth disilicates (Y,Yb,Lu)2Si2O7 in the presence of Al(OH)3 impurities, J. Eur. Ceram. Soc. 27 (2007) 2705–2713, https://doi.org/10.1016/j.jeurceramsoc.2006.09.013.
[16] L. Dong, M.J. Liu, X. Zhang, K. Zhou, Low temperature in-situ formation of oxygen barriers by heat treatment of aluminum infiltrated environmental barrier coatings, Ceram. Int. 47 (2021) 34463–34472, https://doi.org/10.1016/j.ceramint.2021.08.360.
[17] C.A. Schneider, W.S. Rasband, K.W. Eliceiri, NIH Image to ImageJ: 25 years of image analysis, Nat. Methods 9 (2012) 671–675, https://doi.org/10.1038/nmeth.2089.
[18] H.M. Rietveld, A profile refinement method for nuclear and magnetic structures, J. Appl. Crystallogr. 2 (1969) 65–71, https://doi.org/10.1107/s0021889869006558.
[19] R. Castaing, Electron probe microanalysis, Adv. Electron. Electron. Phys. 13 (1960) 317–386, https://doi.org/10.1016/S0065-2539(08)60212-7.
[20] K.N. Lee, D.L. Waters, B.J. Puleo, A. Garg, W.D. Jennings, G. Costa, D. E. Sacksteder, Development of oxide-based high temperature environmental barrier coatings for ceramic matrix composites via the slurry process, J. Eur. Ceram. Soc. 41 (2021) 1639–1653, https://doi.org/10.1016/J.JEURCERAMSOC.2020.10.012.
[21] R.M. German, P. Suri, S.J. Park, Review: liquid phase sintering, J. Mater. Sci. 44 (2009) 1–39, https://doi.org/10.1007/s10853-008-3008-0.
[22] Y. Fan, M. Lai, J. Zhao, Y. Yao, L. Yang, Y. Liu, Y. Li, Q. Li, B. Liu, Theoretical investigation of formation and diffusion mechanisms for point defects in ytterbium and lutetium silicates, J. Am. Ceram. Soc. 105 (2022) 653–667, https://doi.org/10.1111/JACE.18069.
[23] M. Wada, T. Matsudaira, N. Kawashima, M. Takeuchi, D. Yokoe, T. Ogawa, T. Kato, M. Takata, S. Kitaoka, Effect of water vapor on mass transfer in polycrystalline Yb2Si2O7 under oxygen potential gradients at high temperatures, Acta Mater. 201 (2020) 373–385, https://doi.org/10.1016/j.actamat.2020.10.002.
[24] H. Xiang, Z. Feng, Y. Zhou, Mechanical and thermal properties of Yb2SiO5: First-principles calculations and chemical bond theory investigations, J. Mater. Res. 29 (2014) 1609–1619, https://doi.org/10.1557/jmr.2014.201.
[25] H. Klemm, Silicon nitride for high-temperature applications, J. Am. Ceram. Soc. 93 (2010) 1501–1522, https://doi.org/10.1111/J.1551-2916.2010.03839.X.

[26] L. Glasser, Thermodynamic consistencies and anomalies among end-member lanthanoid garnets, J. Chem. Thermodyn. 78 (2014) 93–98, https://doi.org/10.1016/j.jct.2014.06.013.
[27] T. Ogawa, N. Otani, T. Yokoi, C.A.J. Fisher, A. Kuwabara, H. Moriwake, M. Yoshiya, S. Kitaoka, M. Takata, Density functional study of the phase stability and Raman spectra of Yb $_2$ O $_3$, Yb $_2$ SiO $_5$ and Yb $_2$ Si $_2$ O $_7$ under pressure, Phys. Chem. Chem. Phys. 20 (2018) 16518–16527, https://doi.org/10.1039/C8CP02497A.
[28] M. Fritsch, H. Klemm, M. Herrmann, B. Schenk, Corrosion of selected ceramic materials in hot gas environment, J. Eur. Ceram. Soc. 26 (2006) 3557–3565, https://doi.org/10.1016/j.jeurceramsoc.2006.01.015.
[29] E.J. Opila, Thermodynamics and kinetics of gaseous metal hydroxide formation from oxides relevant to power and propulsion applications, Calphad 55 (2016) 32–40, https://doi.org/10.1016/J.CALPHAD.2016.06.007.
[30] J. Leitner, P. Voňka, D. Sedmidubský, P. Svoboda, Application of Neumann–Kopp rule for the estimation of heat capacity of mixed oxides, Thermochim. Acta 497 (2010) 7–13, https://doi.org/10.1016/J.TCA.2009.08.002.
[31] X. Wang, H. Xiang, X. Sun, J. Liu, F. Hou, Y. Zhou, Thermal properties of a prospective thermal barrier material: $Yb_3Al_5O_{12}$, J. Mater. Res. (2022), https://doi.org/10.1557/jmr.2014.319.
[32] R.A. Robie, B.S. Hemingway, Thermodynamic properties of minerals and related substances at 298.15 K and 1 bar (10^5 pascals) pressure and at higher temperatures (1995), https://doi.org/10.3133/b2131.
[33] A.V. Plyasunov, Thermodynamic properties of H4SiO4 in the ideal gas state as evaluated from experimental data, Geochim. Cosmochim. Acta 75 (2011) 3853–3865, https://doi.org/10.1016/j.gca.2011.04.016.